

**PCCP****Ligand induced shape transformation of thorium dioxide nanocrystals**

Journal:	<i>Physical Chemistry Chemical Physics</i>
Manuscript ID	CP-ART-01-2018-000240.R2
Article Type:	Paper
Date Submitted by the Author:	07-Apr-2018
Complete List of Authors:	Wang, Gaoxue; Los Alamos National Laboratory, Theoretical Division Batista, Enrique; Los Alamos National Laboratory, Yang, Ping; Los Alamos National Laboratory, Theoretical Division

SCHOLARONE™
Manuscripts

**Ligand induced shape transformation of
thorium dioxide nanocrystals**

Gaoxue Wang, Enrique R. Batista and Ping Yang*

Los Alamos National Laboratory, Los Alamos, NM 87544

(April 6, 2018)

*Corresponding author: pyang@lanl.gov

Abstract

Nanocrystals (NCs) with size and shape dependent properties are a thriving research field. Remarkable progress has been made in the controlled synthesis of NCs of stable elements in the past two decades, however, the knowledge on the NCs of actinide compounds has been considerably limited due the difficulties in handling them both experimentally and theoretically. Actinide compounds, especially actinide oxides, play a critical role in many stages of nuclear fuel cycle. Recently, a non-aqueous surfactant assisted approach has been developed for the synthesis of actinide oxide NCs with different morphologies, but an understanding of its control factors is still missing to date. Herein we present a comprehensive study on the low index surfaces of thorium dioxide (ThO_2) and their interactions with relevant surfactant ligands using density functional calculations. A systematic picture on the thermodynamic stability of ThO_2 NCs in different size and shape is obtained employing the empirical models based on the calculated surface energies. It is found that bare ThO_2 NCs prefer the octahedral shape terminated by (111) surfaces. Oleic acid displays selective adsorption on the (110) surface, leading to the shape transformation from octahedrons to nanorods. Other ligands such as acetylacetone, oleylamine, and trioctylphosphine oxide do not modify the equilibrium shape of ThO_2 NCs. This work provides atomic level insights into the anisotropic growth of ThO_2 NCs that was recently observed in experiments, thus may contribute to the controlled synthesis of actinides oxides NCs with well-defined size and shape for future applications.

Introduction

Actinide compounds, especially actinide oxides, have been widely used in traditional nuclear fuel fabrication and play an important role in many stages of the nuclear fuel cycle^{1, 2}. Growing evidence suggests nanostructured nuclear fuel is a potentially high-performing option, possessing enhanced radiation fuel stability against restructuring at medium-to-high burnups³⁻⁶. Moreover, the nuclear fuel recrystallizes into High Burn-up Structures (HBS) with grains size at nanoscale after irradiation. Nanocrystals (NCs) of actinide oxides can serve as models to study the properties of nuclear wastes and their migration in nearby geological environments⁶. However, the size and shape effects on the physical and chemical properties of actinide oxide NCs have been poorly explored mainly due to the challenges in handling the radioactive and toxic actinides in experiments and the complexity in treating the 5f electrons in theory. Our knowledge on actinide oxide NCs is lagging far behind what is known for NCs of main-group elements. Recently, the non-aqueous surfactant assisted synthesis has been utilized for the synthesis of actinide oxide nanocrystals (ThO₂, UO₂, and NpO₂) yielding NCs with different morphologies, such as branched nanocrystals, nanodots, and nanorods⁷⁻¹⁰. The non-aqueous colloidal synthesis of UO₂ NCs was first proposed by Cao and co-workers using uranyl acetylacetonate (UO₂(acac)₂) as the precursor and a mixture of organic media including oleic acid (OA)/oleylamine (OAm)/octadecene (ODE)¹⁰. Later, the method was extended to synthesize other actinide oxide NCs such as ThO₂ and NpO₂ by Hudry et al. in organic media of dibenzyl ether (BnOBn)/OA/OAm, or BnOBn/OA/trioctylamine (N(Oct)₃)/trioctylphosphine oxide (OP(Oct)₃)⁷⁻⁹. Despite these pioneering experimental works, the underlying mechanism that controls the morphologies of actinide oxides NCs is still unclear.

The past two decades have witnessed an exponential growth of activities in the synthesis of nanomaterials with main-group elements, driven by both the exciting new science and the great prospects for various applications including solar energy conversion, light emission, catalysts, and electronic devices etc.¹¹⁻¹⁴ NCs, typically under 100 nanometers in diameter, are one of the most investigated families of nanomaterials. They frequently exhibit a wide range of physical and chemical properties that are different from their molecular or bulk counterparts. Due to quantum

confinement effects and large surface-to-volume ratio^{13, 15}, the properties of NCs depend sensitively on both their size and shape, rendering great flexibility in tuning their properties for versatile applications.

Spectacular success has been made in developing a myriad of methods to synthesize NCs of main-group elements¹⁶⁻¹⁹. In particular, the wet chemical or solution method is a convenient and reproducible route suited for tailoring the size, shape and composition of NCs of noble metal and quantum dots^{13, 15, 20-22}. It is well-known from the wet chemical synthesis that surfactant ligands play important roles in determining the structure and the properties of NCs^{19, 23-26}. Firstly, the binding of surfactant ligands to the surfaces of NCs saturates the dangling bonds and may modify the kinetics of the nucleation and growth processes²³. Secondly, the selective adhesion of ligands to a particular surface may modify the thermodynamic stability of NCs in different shapes²⁷. Moreover, ligands influence the optical and electronic properties of NCs. Last but not least, the steric interaction of the surfactant ligands ensure the synthesis of monodisperse NCs^{23, 28}. Therefore, to improve the controlled synthesis of actinide oxide NCs, we have to gain better understandings on the atomic structure of the surfaces and ligand-surface interactions for actinide oxides. However, it is challenging to gain such information experimentally due to the complexity of the synthetic conditions and the unavailability of robust experimental techniques. In contrast, density functional theory (DFT) is a powerful tool for studying the surfaces and ligand-surface interactions. In particular, the combination of DFT calculations with the empirical models such as Wulff construction could provide invaluable information on the shape of NCs^{19, 29}.

In this paper, we focus on ThO₂ that is a promising alternative for UO₂ nuclear fuel because of its higher natural abundance, thermal conductivity, melting point, and chemical stability than the conventional UO₂ fuel³⁰. ThO₂ has also been used as support for single atom catalysts³¹. We perform a systematic DFT study on the surfaces of ThO₂ and their interactions with surfactant ligands. Based on the calculated surface energies, we compare the thermodynamic stability of ThO₂ NCs in different shapes and evaluate the effects of capping ligands on the stability of NCs employing the Wulff construction and a thermodynamic model proposed by Barnard and Zapol³². The calculated results highlight the important role of surface-ligand interactions in

determining the equilibrium shape of ThO₂ NCs. This study improves our understanding on the thermodynamic stability of ThO₂ NCs, and will pave the way to a comprehensive understanding of the formation and growth of other actinide oxides NCs.

Computational methods

Electronic structure calculations

The calculations were performed with the use of DFT and projector augmented-wave (PAW) method³³ as implemented in the Vienna *ab initio* Simulation Package (VASP)³⁴. The generalized gradient approximation (GGA) of Perdew-Burke-Ernzerhof (PBE)³⁵ functional was used to represent the exchange-correlation interaction. The valence electrons were treated with a scalar relativistic approach without inclusion of spin-orbit interaction (SOI) since it has been demonstrated that SOI has negligible effects on the surface energies of thorium dioxide³⁶. Plane wave basis sets with a cutoff energy of 500 eV were employed³³. The energy convergence was set to 10⁻⁶ eV and the residual force on each atom was smaller than 0.01 eV/Å for the structural relaxation. Since density functional theory could not capture the van der Waals (vdW) interactions between the ligand and the surface, the DFT-D3 method of Grimme was included in the calculations³⁷. Bulk ThO₂ has a fluorite structure³⁸, our calculations find a lattice constant of 5.62 Å in good agreement with the experimental value of 5.60 Å³⁹. The calculated electronic band gap of ThO₂ is 4.38 eV which is consistent with previously reported value of 4.52 eV at GGA-PBE level of theory⁴⁰.

Surface energies

The surface of ThO₂ was represented by slab models with periodic boundary conditions in the lateral direction and a vacuum region normal to the surface. The surface energy γ_{clean} for a clean surface was defined as⁴¹

$$\gamma_{clean} = \frac{1}{2A}(E_{slab} - N_{Th}\mu_{Th} - N_O\mu_O) \quad (1),$$

where E_{slab} is the total energy of the relaxed slab, μ_{Th} and μ_O are the chemical potential of the Th atom and O atom, respectively. N_{Th} and N_O are the number of Th atoms and O atoms in the slab. A is the surface area. γ_{clean} can be considered as the required energy for creating the surface from the bulk materials, the most stable surface minimizes γ_{clean} . Since the surfaces are in equilibrium with the underlying bulk material, the chemical potential μ_{Th} and μ_O are not independent, they are related through the equation⁴¹

$$\mu_{Th} + 2\mu_O = E_{ThO_2}^{bulk} \quad (2),$$

where $E_{ThO_2}^{bulk}$ is the calculated energy of bulk ThO₂ per unit formula. Thus, the surface energy in Eq. 1 can be rewritten as

$$\gamma_{clean} = \frac{1}{2A} (E_{slab} - N_{Th}E_{ThO_2}^{bulk} + (2N_{Th} - N_O)\mu_O) \quad (3).$$

We have considered the low Miller index (111), (110) and (100) surfaces with stoichiometry ($N_{Th} = 2N_O$), hyper-stoichiometry ($N_{Th} < 2N_O$) and hypo-stoichiometry ($N_{Th} > 2N_O$). The convergence of surface energies with respect to the thickness of the slab, the number of k -points, and the thickness of the vacuum region has been carefully checked (Figure S1 in the Supplementary Materials).

Considering the physical limitations on the chemical potentials, μ_O can only take the values in the range⁴¹

$$\frac{E_{ThO_2}^{bulk} - E_{Th}^{bulk}}{2} < \mu_O < \frac{E_{O_2}^{mol}}{2} \quad (4).$$

It is convenient to define $\Delta\mu_O = \mu_O - \frac{E_{O_2}^{mol}}{2}$, in this way the upper limit of $\Delta\mu_O$ equals to 0, and the lower limit of $\Delta\mu_O$ equals to half of the formation energy of ThO₂, $\frac{1}{2}E_F^{ThO_2}$. The calculated formation energy of ThO₂ is -12.81 eV, which is good agreement with the experimental value of -12.71 eV^{42, 43}. Therefore, we have

$$-6.41 \text{ eV} = \frac{1}{2}E_F^{ThO_2} = \frac{E_{ThO_2}^{bulk} - E_{Th}^{bulk} - E_{O_2}^{mol}}{2} < \Delta\mu_O < 0 \quad (5).$$

Wulff construction

Wulff construction is a popular approach to build the equilibrium shape of NCs⁴⁴. The basic concept of Wulff construction is to minimize the total surface energy of NCs at a given volume. During the growth of NCs, the high-energy facet grows faster than the low-energy facets, consequently, the high-energy facets will eventually vanish, leading to NCs terminated with low-energy facets. It has been proved that the total surface energy is minimized when the distance (h_i) of a specific surface to the center of the NC is proportional to its surface energy (γ_i)⁴⁵

$$\frac{\gamma_i}{h_i} = \text{constant} \quad (6).$$

Using the calculated surface energies for different facets, one can construct the shape of NCs according to Eq. 6. In this work, the open source code SOWOS was used for Wulff construction⁴⁶. Whereas Wulff construction is invaluable to interpret the equilibrium shape of NCs, the size and surface tension effects are ignored in this model. These effects become important for NCs with a diameter of a few nanometers. Therefore, we have also employed the thermodynamic model proposed by Barnard and Zapol³² to account for the size and surface tension effects. This model has been successfully used to explain the anatase-to-rutile phase transition of TiO₂ NCs depending on the adsorbed groups on the surfaces⁴⁷. It is based on minimization of the total free energy of NCs³²

$$G = \Delta_f G_x + \frac{M}{\rho} (1 - e) [q \sum_i f_i \gamma_i] \quad (7),$$

where $\Delta_f G_x$ is the free energy of formation of bulk ThO₂ which equals to -1236.17 kJ/mol (~12.81 eV) according to our calculations, and the experimental value is -1226.4 kJ/mol (~12.71 eV)^{42, 43}. M is the molar mass, ρ is the density of the material, γ_i and f_i are the surface energy and the weighting factor of the facet i , and q is the surface-to-volume ratio that is related to the shape and size of the NC. e is the volume dilation induced by the surface tension σ ³², which can be calculated with

$$e = \frac{2\beta\sigma}{R} \quad (8),$$

where β is the material compressibility, R is the mean radius of the NCs. The surface tension is approximated by the surface energy $\sigma \approx \gamma$ ³². It should be noted

that the edge energy and the corner energy are neglected in the calculation of the total free energy in this work.

Ligand-surface interactions

To evaluate the effects of capping ligands on the shape of NCs, the binding energies of ligands on different surfaces of ThO₂ were calculated. The binding energy of a ligand on a particular surface was defined as

$$E_b = E_{slab+ligand} - E_{slab} - E_{ligand} \quad (9),$$

where $E_{slab+ligand}$ is the total energy of the composite system, E_{slab} and E_{ligand} are the energy of the isolated slab and the ligand, respectively. By this definition, a negative value of E_b corresponds to an exothermic process, which means the ligand will spontaneously adsorb on the surface, thus stabilize the surface. In contrast, a positive value indicates that the ligand will not adsorb on the surface. The surface energy upon ligand adsorption was defined as

$$\gamma = \gamma_{clean} + \Theta \times E_b \quad (10),$$

where Θ is the coverage of the ligand on the surface (the number of adsorbed ligands per unit area). It is seen from Eq. 10, that the surface energy upon the adsorption of ligands depends on the surface energy of the clean surface, the binding energy as well as the coverage of ligands on the surface. The binding energy E_b is also dependent on the coverage of ligands, especially at a large coverage of ligands due to the steric effects. The adsorption of ligands to a facet of NCs modifies its surface energy, thus influencing the growth rate of this facet and the final shape of the NCs^{23, 25}. From a kinetic perspective, the adsorption of ligand on a particular facet will prevent the deposition of actinide atoms on this surface, thus slows the growth rate of this facet and eventually influences the shape of NCs.

We have considered four surfactant ligands including OA, OAm, trioctylphosphine oxide (OP(Oct)₃), acetylacetone (acac). OA, OAm and OP(Oct)₃ were selected according to the organic media used in the experiments, acac was selected because of its presence in the precursor Th(acac)₄⁷⁻⁹. In the simulations, smaller ligands acetic acid, methylamine, and trimethylphosphine oxide (OP(Methyl)₃) with the same

functional groups were used to mimic the large ligand molecules OA, OAm and OP(Oct)₃, respectively (Figure S2 in the Supplementary Materials). These smaller ligands could capture the nature of chemical bonding interactions between ligands and the surfaces, which allows us to calculate the binding energies at reduced computational costs. This strategy has been widely used in the literatures to elucidate the interaction of ligand with the surface of transition metals and semiconductors^{27, 48}. One obvious limitation of this model is that the steric effects from the long tails of the ligands are ignored, which becomes nontrivial at a large ligand coverage²⁷. To account for the steric effects, we have added a correction term $\Delta_{correction}$ in the calculation of the binding energy

$$E_b = E_{slab+ligand} - E_{slab} - E_{ligand} - \Delta_{correction} \quad (11).$$

The details for the calculation of $\Delta_{correction}$ can be found in the Supplementary Materials. For the investigated ligands, the calculated steric correction is given in Figure S4 in the Supplementary Materials. The steric correction is relatively small at a small coverage of ligands (less than 1 eV for the coverage of ligands smaller than ~ 4 ligands/nm² for OA and OAm, ~ 3 ligands/nm² for acac, and ~ 1.5 ligands/nm² for OP(Oct)₃), and increases significantly at a larger coverage as a result of the repulsion between the ligands.

Results and discussion

Clean surfaces

The clean surfaces were obtained by cleaving from the bulk ThO₂. Figure 1 shows the relaxed structures of stoichiometric (111), (110) and (100) surfaces. The (110) surface is nonpolar and composed of neutral ThO₂ plane (Figure 1(b)). Conversely, the (111) and (100) surfaces are polar surfaces composing of a stacking sequence of charged O and Th planes (Figures 1(a) and 1(c)). The polar (111) and (100) surfaces are terminated with the O atoms to fulfill the polarity compensation criterion⁴⁹. On the (111) surface, the topmost O₍₁₎ atoms are 3-fold coordinated, and the Th₍₂₎ atoms are 7-fold coordinated. On the (110) surface, the topmost O₍₁₎ atoms are 3-fold coordinated and the Th₍₂₎ atoms have a coordination number of 6. On the (100) surface, the O₍₁₎ atoms have a coordination number of 2, and the Th₍₂₎ atoms have a

coordination number of 6. The calculated surface energies are shown in Figure 2(a). It is found that the stoichiometric surfaces are energetically more stable than the hyper- or hypo-stoichiometric surfaces in the allowed the chemical potential range. For the stoichiometric surfaces, the surface energies of (111), (110), and (100) are 50, 75, 110 $\text{meV}/\text{\AA}^2$, respectively. A comparison of the surface energies from our calculations and the values reported in the literatures are summarized in Table S1 in the Supplementary Materials. The good agreement with the reported values demonstrates the reliability of our calculations^{36, 50, 51}. The equilibrium shape of clean NCs built with Wulff construction based on the calculated surface energies is shown in Figure (b). Not surprisingly, ThO_2 prefers to form octahedral NCs exposing the (111) facet due to its lower surface energy.

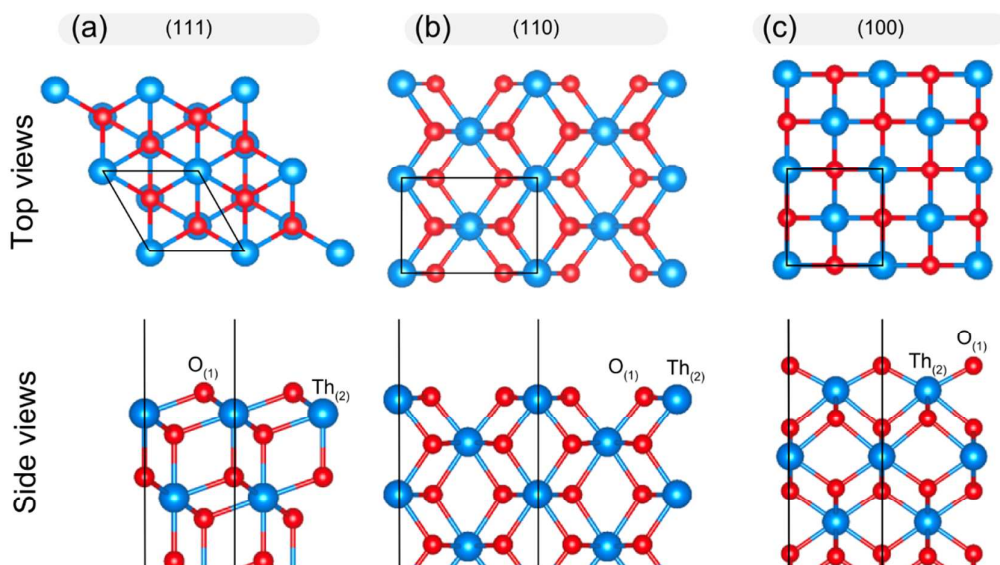


Figure 1. Top and side views of the stoichiometric (111), (110), and (100) surfaces of ThO_2 . The topmost O and Th atoms are labeled as $\text{O}_{(1)}$ and $\text{Th}_{(2)}$, respectively.

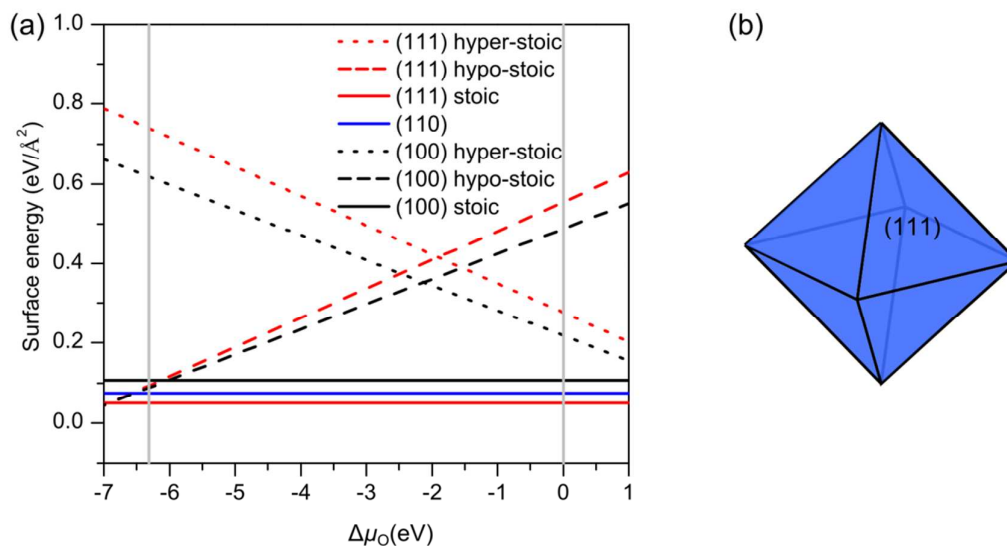


Figure 2. (a) Surface energies of stoichiometric, hyper-stoichiometric and hypo-stoichiometric (111), (110), and (100) surfaces of ThO₂, (b) Wulff construction of the ThO₂ NCs. The vertical lines in (a) represent the lower and upper limitations for Δμ_O.

Ligand-surface interactions

The adsorption of ligands on the surfaces of ThO₂ was simulated by optimizing various initial configurations. For acetic acid and acac ligands, nine different initial structures were considered as illustrated in Figure S5 in the Supplementary Materials. For methylamine, four different initial configurations were considered as illustrated in Figure S6 in the Supplementary Materials. For OP(Methyl)₃, only one initial configuration was considered with the O atom of the ligand directly above one surface Th site.

Figures 3 and 4 show the most stable adsorption configurations of acetic acid and acac ligands on the stoichiometric (111), (110) and (100) surfaces of ThO₂. Both acetic acid and acac ligands experience dissociative adsorption with one proton moving to a nearby O site. The acetic acid ligand has the binding energy of -2.53 eV on the (110) surface, in contrast, the binding energy on the (111) and (100) surfaces is much smaller, which is -1.26 eV and -1.81 eV, respectively. The adsorption of acac also has the strongest binding strength on the (110) surface with binding energy of -3.09 eV, while on the (111) surface the binding energy is -2.21 eV. The selective adsorption of

acetic acid and acac ligands is attributed to the differences in the surfaces structures. The thorium atoms on the (110) surface have a lower coordination number of 6 as compared to 7 on the (111) surface, allowing the ligands to bond more strongly with the (110) surface. Moreover, the (110) surface has a flat surface with Th and O atoms on the same plane, while the topmost layer of (111) and (100) surfaces are O atoms contributing to stronger repulsion between the O atoms of the ligands and the surfaces. Acac displays a smaller difference in the binding energies on (111) and (110) surfaces as compared to acetic acid due to different binding forms on the surfaces. Acac adsorbs on both the (111) and (110) surfaces in the bidentate bridging form as seen in Figures 4(a) and 4(b), while acetic acid adsorbs in the bidentate bridging form on the (110) surface and in the monodentate form on the (111) surface as seen in Figures 3(a) and 3(b). In general, the binding energies of the bidentate bridging form are larger than that of the monodentate form on the same surface (see Figures S7 (b), (c) and (d), the energy difference is in the range of 0.49~0.76 eV). The exception is the acetic acid ligand on the (111) surface (see Figure S7(a)) where the monodentate form is slightly more stable than the bidentate bridging form. This is due to the smaller $O_{\text{ligand}}-O_{\text{ligand}}$ distance of 2.27 Å in acetic acid compared to 2.65 Å in acac resulting in stronger repulsion between the O atoms of the (111) surface and O atoms of the ligands, thus leads to longer $O_{\text{ligand}}-\text{Th}_{\text{surface}}$ bond length of 2.66 and 2.68 Å as compared to 2.49 and 2.52 Å on the (110) surface (see Table S2 in the Supplementary Materials). The selective adsorption has paramount influence on the equilibrium shape of the NCs as will be shown in the next section.

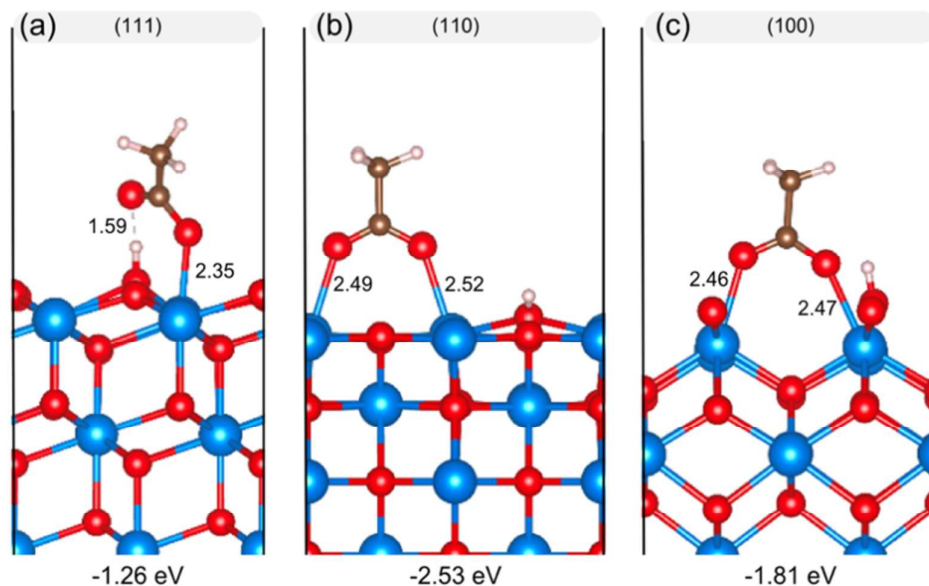


Figure 3. Adsorption configurations and the corresponding binding energies of acetic acid on (111), (110) and (100) surfaces of ThO_2 . The bond length is in unit of Å .

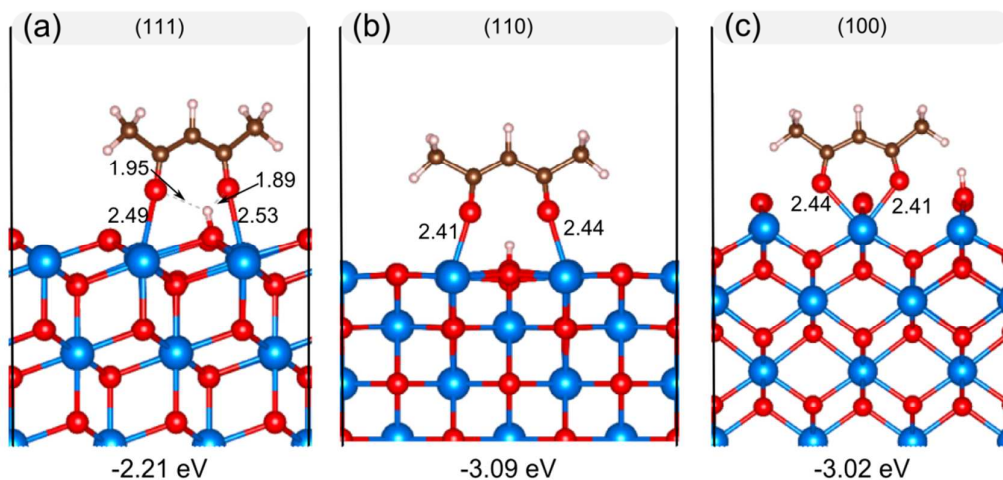


Figure 4. Adsorption configurations and the corresponding binding energies of acac on (111), (110) and (100) surfaces of ThO_2 . The bond length is in unit of Å .

Figures 5 and 6 show the most stable adsorption configurations of methylamine and the $\text{OP}(\text{Methyl})_3$ on different surfaces of ThO_2 . The methylamine and the $\text{OP}(\text{Methyl})_3$ have relatively weaker binding energies smaller than -1.0 eV. The N or O atom in the ligands bonds with one of Th atom of the surface. Different from the acetic acid and acac ligands, the binding energy of methylamine or $\text{OP}(\text{Methyl})_3$ on different surfaces shows very small variation in the range from -0.7 to -1.0 eV

suggesting these two ligands will not influence the equilibrium shape of the ThO_2 NCs.

The ligand-surface interaction can be understood based on the covalent bond classification (CBC)^{28, 52, 53}, where the ligands are classified as L-, X-, or Z-type depending on the number of electrons that the ligand contributes to the ligand-surface bond (2, 1 or 0 respectively). Following this classification, acetic acid and acac are X-type ligands which donate one electron and attract another electron from the surface to form covalent ligand-surface bonds. They have stronger binding strength on the surfaces of ThO_2 due to the formation of covalent chelate bonds. While methylamine and $\text{OP}(\text{Methyl})_3$ are the L-type ligands, they are two electron donors with a lone electron pairs coordinate with one Th atom of the surface to form weaker dative bonds. They display similar binding strength on various surfaces of ThO_2 .

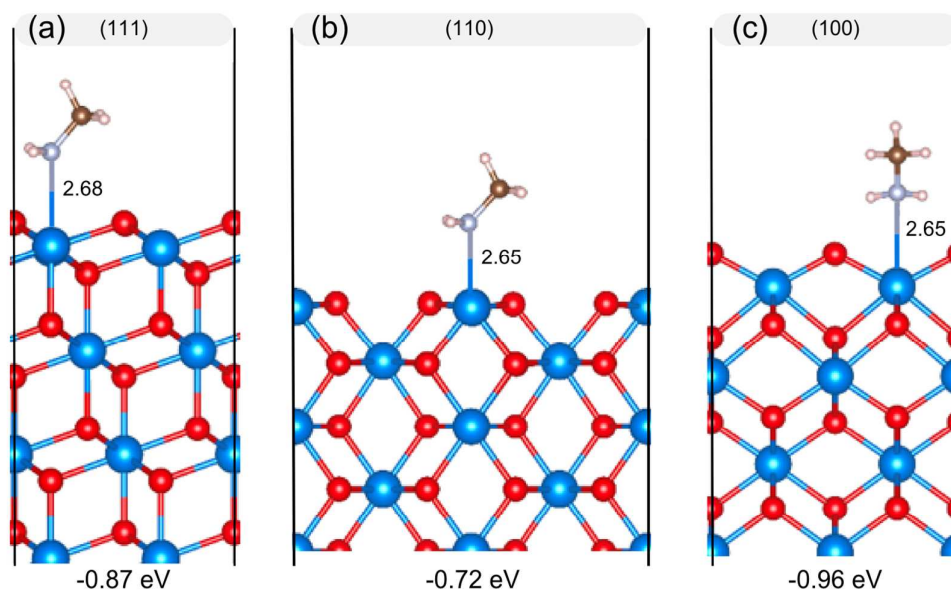


Figure 5. Adsorption configurations and the corresponding binding energies of methylamine on (111), (110) and (100) surfaces of ThO_2 . The bond length is in unit of Å.

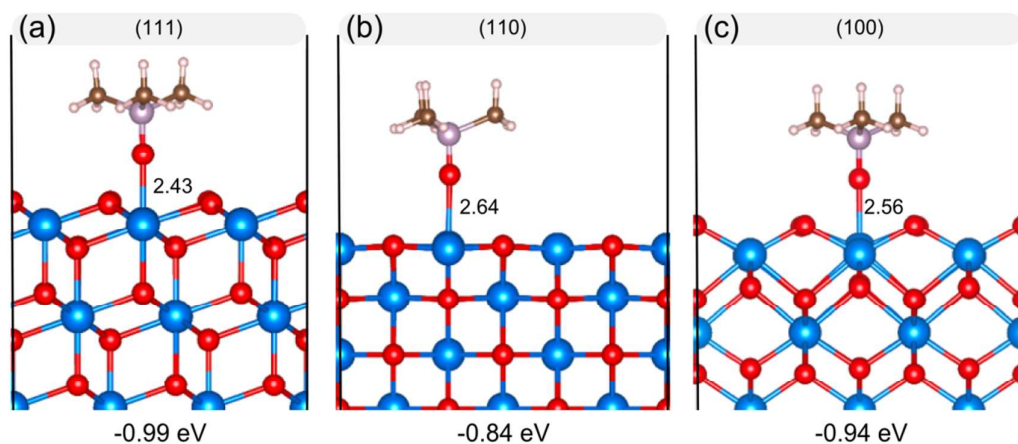


Figure 6. Adsorption configurations and the corresponding binding energies of $OP(\text{Methyl})_3$ on (111), (110) and (100) surfaces of ThO_2 . The bond length is in unit of \AA .

Effects of surfactant ligand on the shape of NCs

Figures 7(a)-(d) show the surface energies as a function of ligands coverage calculated with Eq. 10. A few important observations can be obtained from these figures. (i) The surface energies decrease with the coverage of the ligands. This is due to the fact that these ligands have negative binding energies on the surface, thus the adsorption of ligands could stabilize the surfaces of ThO_2 , and reduce the surface energies. (ii) The surface energy decreases at different rates with the adsorption of OA or acac ligand, while at a similar rate with the adsorption of OAm or $OP(\text{Oct})_3$. This is related to the variation of the binding energies of the ligand on different surfaces of ThO_2 . OA and acac show selective adsorption on the (110) surface with a larger binding energy than that on the (111) and (100) surfaces, thus the surface energy of the (110) surface decreases at a higher rate. While OAm or $OP(\text{Oct})_3$ has similar binding energy on different surfaces resulting in similar decreasing rate of the surface energy. (iii) A crossover is observed for the surface energy of (110) and (111) surfaces with OA adsorption at ~ 2.0 ligands/ nm^2 as seen from Figure 7(a). The (111) surface is the most stable facet at a small coverage of OA, while the (110) surface becomes the most stable facet when the coverage of OA is larger than ~ 2.0 ligands/ nm^2 . The change of the relative stability of the surface has significant effects on the equilibrium shape of the ThO_2 NCs as show in Figure 7(e). Without ligands adsorption ($\theta = 0$), the octahedron is the most stable shape for the ThO_2 NCs exposing only the (111) surface; when increasing the coverage of OA to $\theta = 2$

ligands/nm², the (110) surface appears on the surface of the NCs; and the (110) surface eventually dominates at the coverage of $\Theta = 2.5$ ligands/nm². As a result, the shape of the NC transforms from an octahedron to a nanorod. Note that the long axis of the nanorod is along the [001] crystalline direction, and the ratio of the long to short axis increases with the coverage of OA from 2.0 to 2.5 ligands/nm². The ThO₂ NCs in the nanorod structure have been observed in experiments by Hudry et al. by using Th(acac)₄ as the precursor⁷. They have further demonstrated using the XPS and FTIR spectra that the synthesized ThO₂ NCs are stabilized by the OA ligands⁷. Moreover, the long axis of the nanorod of ThO₂ NCs is growing along the [001] direction⁷, which is fully consistent with our simulations. Therefore, OA ligand is playing the shape determining role for the growth of ThO₂ NCs into the nanorod structure. Changing the concentration of OA in the organic media could be a potential approach to tune the shape of the ThO₂ NCs. However, the starting ratio of OA-to-Th in the organic media should be kept smaller than four, as Hudry et al. found that there was no formation of ThO₂ NCs when the ratio was larger than four⁸. This is likely due to the decomposition of the NCs in the excess of OA, which has been reported in the synthesis of cobalt NCs in OA⁵⁴. It is also interesting to notice that the calculated surface energy of (110) and (111) surfaces goes to negative values when the coverage of OA is larger than ~ 2.5 and ~ 2.8 ligands/nm², respectively. The negative surface energy indicates the decomposition of the NCs in excess of OA, which is in line with the experiments⁸.

Acac ligand also exhibits selective adsorption on (110) facet, however, the crossover of the surface energy of (111) and (110) does not occur with the coverage smaller than 3 ligands/nm² (Figure 7(b)). Since the repulsion between the acac ligands increases significantly when the coverage is larger than 3 ligands/nm² (Figure S4(b) in the Supplementary Materials), which limits the coverage of acac on the surface to a value smaller than 3 ligands/nm². Therefore, the concentration of acac is unlikely to modify the equilibrium shape of ThO₂ NCs. For OAm and OP(Oct)₃, since the surface energies decrease at a similar rate with the coverage (Figures 7(c) and 7(d)) of these ligands, thus they do not modify the relative stability of these surfaces and the equilibrium shape of the ThO₂ NCs. Hudry et al. reported that the presence of OAm would prevent the formation of ThO₂ NCs⁸. However, in their experiments, the OA-to-Th ratio was set to ten in the organic media of BnOBn/OA/OAm⁸. As the

excess of OA (the ratio of OA-to-Th larger than four) could also prevent the formation of the ThO_2 NCs, further experiments are necessary to validate the role of OAm for the growth of ThO_2 NCs.

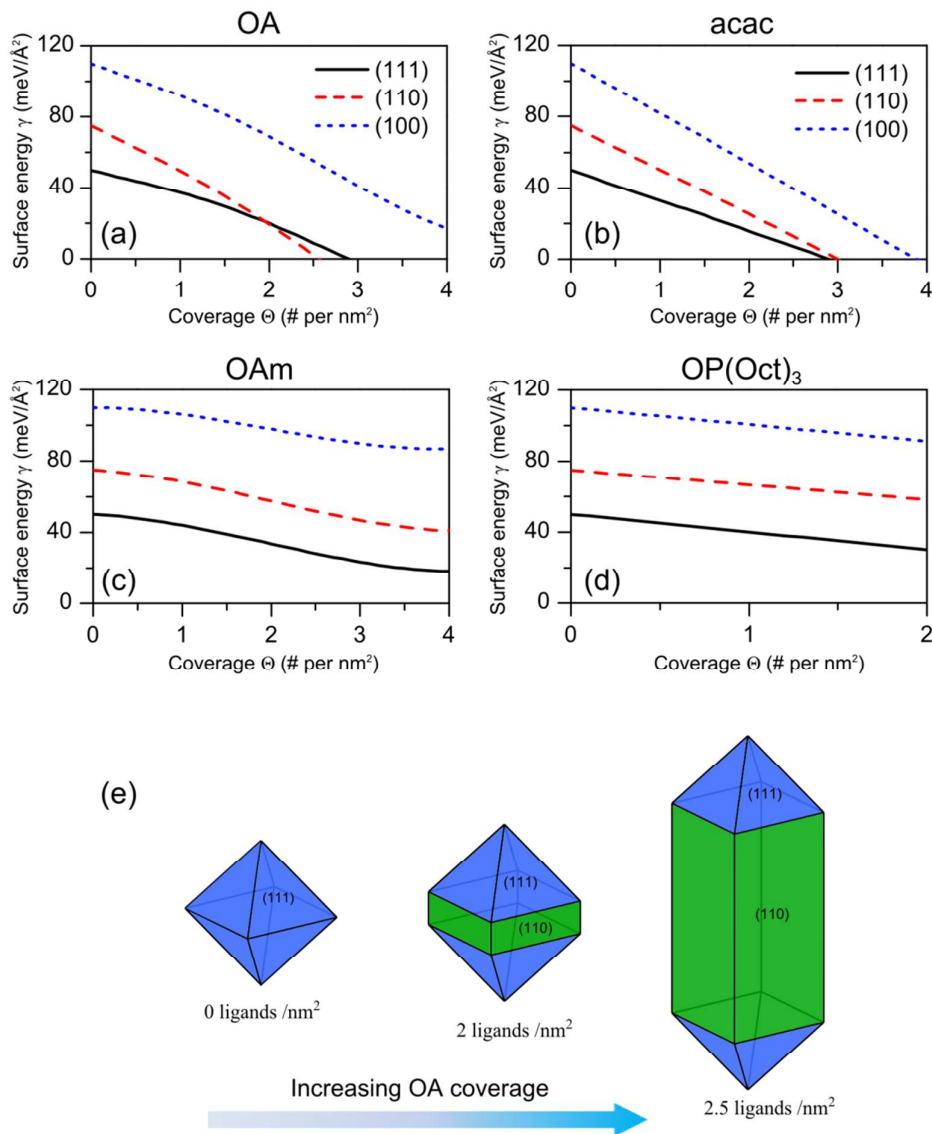


Figure 7. Surface energies of ThO_2 as a function of the coverage of ligands for OA (a), acac (b), OAm (c), $\text{OP}(\text{Oct})_3$ (d), and the evolution of most stable shape of the nanocrystal with increasing coverage of OA (e).

Thermodynamic stability of NCs with different size and shape

In the previous section, we have built the equilibrium shape of ThO_2 nanocrystals based on Wulff construction using the thermodynamics as the driving force. The octahedron structure is found to be the most stable shape for bare ThO_2 NCs, and a

shape transformation to the nanorod is predicted with the adsorption of OA on the surfaces. To gain further knowledge of thermodynamic stability of ThO₂ NCs, we employed the theoretical model proposed by Barnard and Zapol³² to compare the free energy of NCs in different size and shape. We have considered NCs in the size range from 100 to 10000 ThO₂ units, corresponding to the average diameter from to ~2 to ~10 nm. The considered shapes include cube, cuboctahedron, sphere, nanorod, octahedron and truncated octahedron. The sphere shape was simulated by averaging the surface energies of the low index surfaces³². Figure 8 shows the free energies of clean and ligands capped ThO₂ NCs. The predicted sequence of the preferred ThO₂ NCs in different shapes is shown in Figure 9. For the clean ThO₂ NCs as shown in Figures 8(a) and 9(a), the octahedron has the lowest free energy than the NCs in other shapes. The truncated octahedron has the second lowest free energy. For OA capped NCs (Figure 8(b) and Figure 9(b)), the nanorod becomes the most stable structure. This change in the relative stability of NCs is consistent with the previous prediction based on Wulff construction. For acac capped NCs (Figure 8(c) and Figure 9(c)), the octahedron structure is the most stable shape and the nanorod structure becomes the second most stable shape. For OAm and OP(Oct)₃ capped NCs (Figure 8(d, e) and Figure 9(d, e)), the octahedron is always the most stable shape. The cube and the sphere NCs have the highest and second highest free energy for all these cases indicating they are the most unlikely shapes for ThO₂ NCs. Hudry et al. have obtained the ThO₂ NCs in the nanorod shape using Th(acac)₂ as precursors which is consistent with our calculations⁷. However, they also found that when using different precursors, such as Th(OAc)₄ or Th(NO₃)₄·5H₂O, the NCs with branched or nanodot shape were obtained⁸. From our simulations, the nanodot shape is the metastable phase for ThO₂ NCs in the presence of OA, thus the use of different precursors could possibly modify the nucleation and growth kinetics of NCs^{19, 24}, resulting in the formation of metastable NCs.

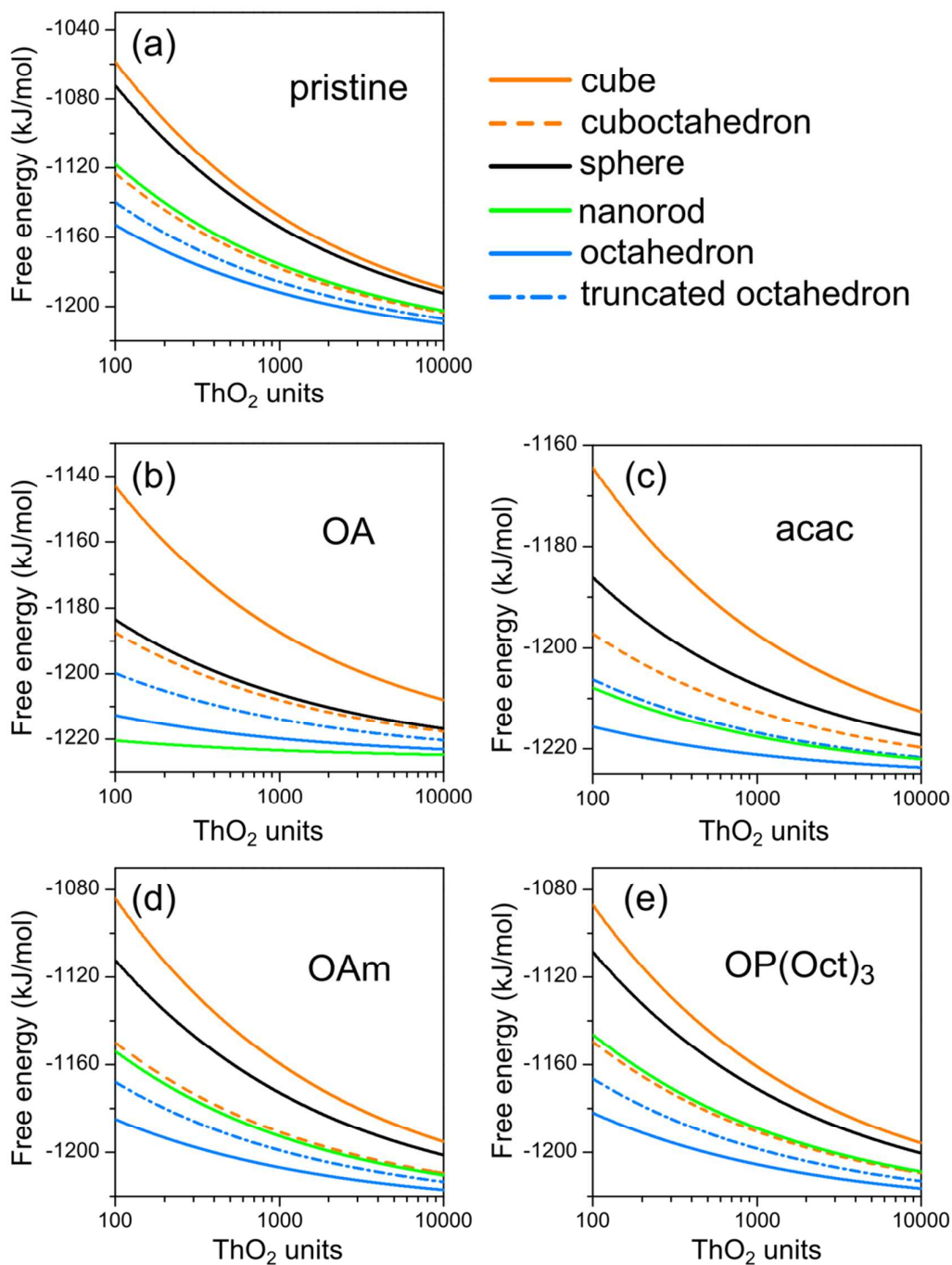


Figure 8. Free energy of different shapes of ThO₂ nanocrystals as a function of size. (a) pristine nanocrystals, (b) OA coverage of 2.5 ligands/nm², (c) acac coverage of 2.5 ligands/nm², (d) OAm coverage of 2.5 ligands/nm², (e) OP(Oct)₃ coverage of 2.0 ligands/nm².

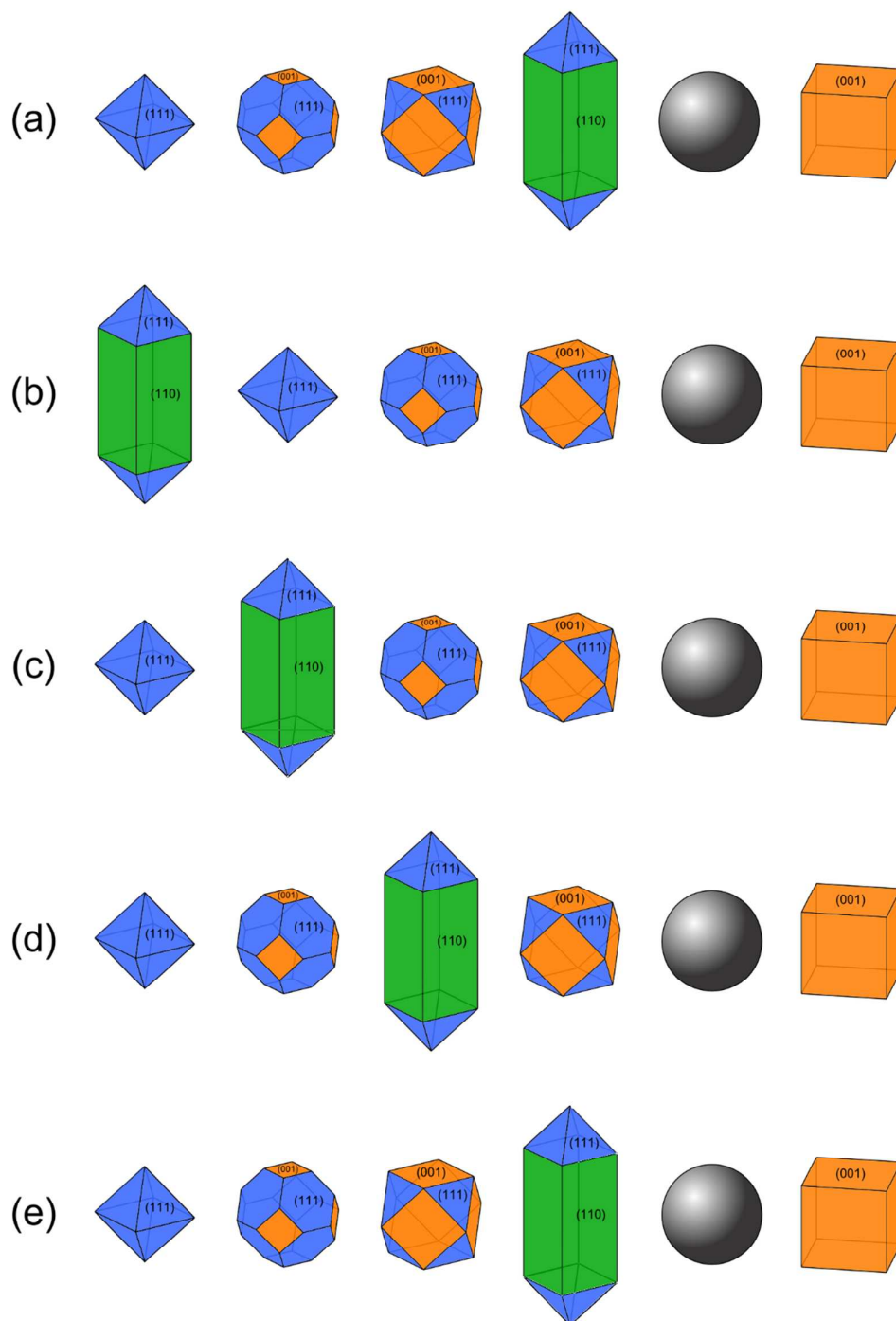


Figure 9. Predicted sequence of the preferred shapes (left to right) for (a) pristine nanocrystals, (b) OA coverage of 2.5 ligands/nm^2 , (c) acac coverage of 2.5 ligands/nm^2 , (d) OAm coverage of 2.5 ligands/nm^2 , (e) $OP(\text{Oct})_3$ coverage of 2.0 ligands/nm^2 .

Summary

In summary, we have presented a density functional study on the clean surfaces of ThO₂, ligands adsorption on the surfaces, and evaluate the effects of ligands on the equilibrium shape of ThO₂ NCs based on thermodynamic models using the calculated surface energies. We have witnessed a shape transformation with increasing the coverage of surfactant ligands on the surface. The bare ThO₂ NCs prefer to form octahedrons exposing the (111) facet. OA ligands exhibit selective adsorption on (110) surface of ThO₂ and induce the shape transformation from octahedrons to nanorods. Therefore, changing the concentration of OA in the synthetic media could be a potential approach to control the shape of the ThO₂ NCs. We have also provided a systematic picture on the thermodynamic stability of ThO₂ NCs in different size and shape, which enriches our understandings on the NCs of actinide oxide. Our calculations explain the anisotropic growth of ThO₂ NCs that was recently observed in experiments, thus may contribute to the controlled synthesis of actinide oxide NCs with well-defined size and shape for applications in novel nanostructured nuclear fuel as well as in studying the migration of radioactive materials in geological environments.

Acknowledgements

The authors gratefully acknowledge funding for this project by the Laboratory Directed Research Development Program of Los Alamos National Laboratory (P.Y.) and the Office of Basic Energy Sciences, Heavy Element Chemistry Program (E.R.B). G.W. thanks the Director's Postdoc Fellowship funded by LANL. Los Alamos National Laboratory is operated by Los Alamos National Security, LLC, for the National Nuclear Security Administration of U.S. Department of Energy (contract DE-AC52-06NA25396). We thank the access to computational resources for this project from the Environmental Molecular Sciences Laboratory of Pacific Northwest National Laboratory in the Cascade supercomputer and LANL's institutional computer, Wolf cluster.

References

1. P. D. Wilson, 1996 (Oxford Univ. Press, Oxford)..
2. J. Fink, *Journal of Nuclear Materials*, 2000, **279**, 1-18.
3. S. Mantoura, *Nature Nanotechnology*, 2006. DOI 10.1038/nnano.2006.202
4. W.-Q. Shi, L.-Y. Yuan, Z.-J. Li, J.-H. Lan, Y.-L. Zhao and Z.-F. Chai, *Radiochimica Acta*, 2012, **100**, 727-736.
5. N. Nita*, R. Schaeublin, M. Victoria and R. Valiev, *Philosophical Magazine*, 2005, **85**, 723-735.
6. J. Spino, H. Santa Cruz, R. Jovani-Abril, R. Birtcher and C. Ferrero, *Journal of Nuclear Materials*, 2012, **422**, 27-44.
7. D. Hudry, C. Apostolidis, O. Walter, T. Gouder, E. Courtois, C. Kübel and D. Meyer, *Chemistry-A European Journal*, 2012, **18**, 8283-8287.
8. D. Hudry, C. Apostolidis, O. Walter, T. Gouder, E. Courtois, C. Kübel and D. Meyer, *Chemistry-A European Journal*, 2013, **19**, 5297-5305.
9. D. Hudry, J.-C. Griveau, C. Apostolidis, O. Walter, E. Colineau, G. Rasmussen, D. Wang, V. S. K. Chakravadhala, E. Courtois and C. Kübel, *Nano Research*, 2014, **7**, 119-131.
10. H. Wu, Y. Yang and Y. C. Cao, *Journal of the American Chemical Society*, 2006, **128**, 16522-16523.
11. G. Cao, *Nanostructures and nanomaterials: synthesis, properties and applications*, World Scientific, 2004.
12. P. G. Bruce, B. Scrosati and J. M. Tarascon, *Angewandte Chemie International Edition*, 2008, **47**, 2930-2946.
13. J. D. Moras, B. Strandberg, D. Suc and K. Wilson, *Science*, 1996, **271**, 933.
14. D. Yu, E. Nagelli, F. Du and L. Dai, *The Journal of Physical Chemistry Letters*, 2010, **1**, 2165-2173.
15. V. F. Puentes, K. M. Krishnan and A. P. Alivisatos, *Science*, 2001, **291**, 2115-2117.
16. J. Park, J. Joo, S. G. Kwon, Y. Jang and T. Hyeon, *Angewandte Chemie International Edition*, 2007, **46**, 4630-4660.
17. X. Peng, L. Manna, W. Yang and J. Wickham, *Nature*, 2000, **404**, 59.
18. J. Park, K. An, Y. Hwang, J.-G. Park, N. Han-Jin, K. Jae-Young, J.-H. Park, N.-M. Hwang and T. Hyeon, *Nature Materials*, 2004, **3**, 891.
19. Y. Xia, X. Xia and H.-C. Peng, *Journal of the American Chemical Society*, 2015, **137**, 7947-7966.
20. W. W. Yu and X. Peng, *Angewandte Chemie International Edition*, 2002, **41**, 2368-2371.
21. X. Peng, J. Wickham and A. Alivisatos, *Journal of the American Chemical Society*, 1998, **120**, 5343-5344.
22. C. Burda, X. Chen, R. Narayanan and M. A. El-Sayed, *Chemical Reviews*, 2005, **105**, 1025-1102.
23. Y. Yin and A. P. Alivisatos, *Nature*, 2005, **437**, 664.
24. Y.-w. Jun, J.-H. Lee, J.-s. Choi and J. Cheon, *The Journal of Physical Chemistry B*, 2005, **109**, 14795-14806.
25. C. R. Bealing, W. J. Baumgardner, J. J. Choi, T. Hanrath and R. G. Hennig, *ACS Nano*, 2012, **6**, 2118-2127.
26. M. Niederberger and R. Deshmukh, *Chemistry-A European Journal*, 2017, **23**, 8542-8570.
27. D. Zherebetsky, M. Scheele, Y. Zhang, N. Bronstein, C. Thompson, D. Britt, M. Salmeron, P. Alivisatos and L.-W. Wang, *Science*, 2014, **344**, 1380-1384.
28. M. A. Boles, D. Ling, T. Hyeon and D. V. Talapin, *Nature materials*, 2016, **15**, 141.
29. G. D. Barmparis, Z. Lodziana, N. Lopez and I. N. Remediakis, *Beilstein Journal of Nanotechnology*, 2015, **6**, 361.
30. J. Belle and R. Berman, *Thorium dioxide: properties and nuclear applications*, USDOE Assistant Secretary for Nuclear Energy, Washington, DC. Office of Naval Reactors, 1984.
31. B. Long, Y. Tang and J. Li, *Nano Research*, 2016, **9**, 3868-3880.
32. A. S. Barnard and P. Zapol, *The Journal of Chemical Physics*, 2004, **121**, 4276-4283.
33. G. Kresse and D. Joubert, *Physical Review B*, 1999, **59**, 1758.
34. G. Kresse and J. Furthmüller, *Computational Materials Science*, 1996, **6**, 15-50.
35. J. P. Perdew, K. Burke and M. Ernzerhof, *Physical Review Letters*, 1996, **77**, 3865.
36. Z. Rák, R. C. Ewing and U. Becker, *Surface Science*, 2013, **608**, 180-187.
37. S. Grimme, *Journal of Computational Chemistry*, 2006, **27**, 1787-1799.

38. V. Kanchana, G. Vaitheeswaran, A. Svane and A. Delin, *Journal of Physics: Condensed Matter*, 2006, **18**, 9615.
39. J. S. Olsen, L. Gerward, V. Kanchana and G. Vaitheeswaran, *Journal of Alloys and Compounds*, 2004, **381**, 37-40.
40. C. Sevik and T. Çağın, *Physical Review B*, 2009, **80**, 014108.
41. K. Reuter and M. Scheffler, *Physical Review B*, 2001, **65**, 035406.
42. R. J. Konings, O. Beneš, A. Kovács, D. Manara, D. Sedmidubský, L. Gorokhov, V. S. Iorish, V. Yungman, E. Shenyavskaya and E. Osina, *Journal of Physical and Chemical Reference Data*, 2014, **43**, 013101.
43. E. J. Huber, C. E. Holley and E. H. Meierkord, *Journal of the American Chemical Society*, 1952, **74**, 3406-3408.
44. G. Wul, *Z. Kristallogr.*, 1901, **34**, 449-530.
45. A. Schöberl and G. Wiehler, *Angewandte Chemie*, 1953, **65**, 33-33.
46. D. Scopece, *Journal of Applied Crystallography*, 2013, **46**, 811-816.
47. A. Barnard and L. Curtiss, *Nano Letters*, 2005, **5**, 1261-1266.
48. Z. Lu, A. Karakoti, L. Velarde, W. Wang, P. Yang, S. Thevuthasan and H.-f. Wang, *The Journal of Physical Chemistry C*, 2013, **117**, 24329-24338.
49. F. Bottin, G. Geneste and G. Jomard, *Physical Review B*, 2016, **93**, 115438.
50. V. Alexandrov, T. Y. Shvareva, S. Hayun, M. Asta and A. Navrotsky, *The Journal of Physical Chemistry Letters*, 2011, **2**, 3130-3134.
51. R. Chatzimichail, S. Bebelis and P. Nikolopoulos, *Journal of Materials Engineering and Performance*, 2016, **25**, 1691-1696.
52. M. L. H. Green and G. Parkin, *Journal of Chemical Education*, 2014, **91**, 807-816.
53. J. De Roo, I. Van Driessche, J. C. Martins and Z. Hens, *Nature Materials*, 2016, **15**, 517-521.
54. A. C. Samia, K. Hyzer, J. A. Schlueter, C.-J. Qin, J. S. Jiang, S. D. Bader and X.-M. Lin, *Journal of the American Chemical Society*, 2005, **127**, 4126-4127.

TOC graphic

